

Interaction Physics of Multipicosecond Petawatt Laser Pulses with Overdense Plasma

A. J. Kemp and L. Divol

Lawrence Livermore National Laboratory, Livermore, California 94551, USA

(Received 7 October 2011; published 9 November 2012)

We study the interaction of intense petawatt laser pulses with overdense plasma over several picoseconds, using two- and three-dimensional kinetic particle simulations. Sustained irradiation with non-diffraction-limited pulses at relativistic intensities yields conditions that differ qualitatively from what is experimentally available today. Nonlinear saturation of laser-driven density perturbations at the target surface causes recurrent emissions of plasma, which stabilize the surface and keep absorption continuously high. This dynamics leads to the acceleration of three distinct groups of electrons up to energies many times the laser ponderomotive potential. We discuss their energy distribution for applications like the fast-ignition approach to inertial confinement fusion.

DOI: [10.1103/PhysRevLett.109.195005](https://doi.org/10.1103/PhysRevLett.109.195005)

PACS numbers: 52.57.Kk, 52.65.Rr

The next generation of petawatt short-pulse laser facilities like NIF-ARC, Omega-EP, or LFEX will deliver multipicosecond, multikilojoule pulses over large focal spots [1–3]. Understanding the interaction physics of such pulses is important to guide future experiments.

Previous theoretical studies of relativistic laser plasma interaction have focused on subpicosecond laser pulses with diffraction-limited focal spots typically less than 10 μm in size [4,5]. Interaction of such pulses with overdense plasma gives rise to Boltzmann-like energy distributions of “hot” electrons peaking near the laser ponderomotive energy $E_p = m_e c^2 (\sqrt{1 + a_0^2} - 1)$, where $a_0 \equiv eB_0/m_e \omega_L$ is the normalized laser field amplitude and ω_L is the laser frequency [6]. While fundamental absorption mechanisms and hot-electron production in short-pulse laser plasma interaction have been studied by many authors [7–10], a global picture of how these will interplay in realistic multipicosecond petawatt laser irradiation of dense plasma is still lacking.

This Letter addresses, for the first time, the long-time evolution of the interaction of realistic petawatt laser pulses with large spot diameters with overdense plasma. We find that the laser interaction causes perturbations of the plasma interface leading to high absorption. We describe how nonlinear saturation of these perturbations leads to recurrent emissions of plasma from the target surface, thus stabilizing the surface while keeping absorption continuously high. This dynamics leads to the acceleration of three distinct groups of electrons up to energies many times the laser ponderomotive potential. We discuss the energy distribution of laser-accelerated electrons and their divergence for applications like the fast-ignition approach to inertial confinement fusion (ICF) [11].

The aim of this Letter is to study the interaction of an energetic laser pulse with overdense plasma over several picoseconds at full scale through kinetic modeling in two- and three-dimensional particle-in-cell simulations [12].

We set up a laser pulse with a transverse flat-top intensity profile $I(r, t) = I_0 \exp[-2(r/r_0)^8] \exp\{-2[(t - 3t_0)/t_0]^2\}$, where $I_0 = 1.37 \times 10^{20} \text{ W/cm}^2$, and a focal spot diameter $2r_0 = 40 \mu\text{m}$, which is much larger than the diffraction-limited spots typically used in current experiments at comparable intensities [13]. This pulse delivers 13 kJ to the target over 10 ps, consistent with fast-ignition requirements [11]; it is linearly polarized in the simulation plane with a wavelength $\lambda_L = 1 \mu\text{m}$ and rise time $t_0 = 200 \text{ fs}$; for $t > 3t_0$, the time-dependent factor is set to 1. We find that it is important to use a realistic rise time to avoid spurious effects. The plasma consists of deuterium ions with mass $M_i = 3672m_e$ and electrons at density $n_0 = 100n_c$, where critical density $n_c = \omega_L^2 m_e / 4\pi e^2 \simeq 1.1 \times 10^{21} \text{ cm}^{-3}$ and $\omega_L = 2\pi c / \lambda_L$. This is sufficient to guarantee $n_0 \gg a_0 n_c$, the density at which intense laser pulses are absorbed. After less than 1 ps, plasma expansion leads to a profile where the bulk density is not accessible to the laser. The simulation box is 140 μm wide and 120 μm long with a Cartesian two-dimensional (2D) geometry, resolved with 50 cells per micron and 116 steps per laser period, with 120 electrons per cell; particles are initialized with a 0.1 keV thermal distribution. Boundary conditions are periodic in the transverse and absorbing for particles and fields in the longitudinal direction. We employ third-order splines for interpolation and a single-pass 2D binary smoothing operator for the current field to reduce numerical self-heating [14].

Figure 1 illustrates the simulation setup and early interaction at 1 ps, i.e., about 0.75 ps after the laser has struck the target, and 3 ps later. The structure of the electron energy flux inside plasma as displayed in Fig. 1(a) is caused by beam filamentation and surface rippling due to electric and magnetic fields on the interaction interface [4,5,15]; these are related to surface waves, filamentary, Rayleigh-Taylor-like, and modulational instabilities [16] that grow on the order of femtoseconds. Transverse gradients of the longitudinal electric field on the target surface

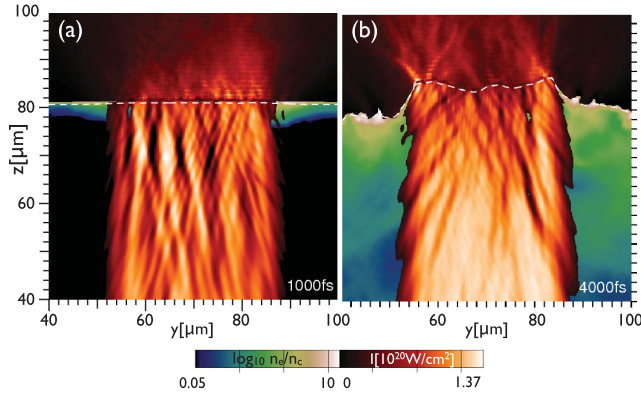


FIG. 1 (color). Relativistic petawatt laser pulse interacting with overdense plasma at 1 ps (a) and at 4 ps (b); the laser pulse is injected at $z = 0$, and plasma is initially at $z > 80 \mu\text{m}$. Energy flux density along z (in red) shows continuously high conversion from the laser into a relativistic electron beam. The dashed line at $n_e = 10n_c$ shows deformation and motion of the absorption layer. Expansion of underdense plasma into vacuum (in green) is evident.

induce perpendicular magnetic fields located at the side walls of filaments. These grow until the geometry of the electric field is locally radially symmetric, so that $|\nabla \times \mathbf{E}| \ll 1$. The resulting “porous” structure of the laser-plasma interface, shown in Figs. 2(a)–2(c), allows ions to move from overdense to underdense regions and to replenish the underdense plasma in front of the target with electrons. In contrast, one-dimensional (1D) simulations predict an electrostatic sheath field near the point of absorption that is structured so that ions cannot escape the bulk plasma [9]. This causes strong density gradient steepening in 1D, which leads to an artificial reduction in absorption over the course of about 1.5 ps under our laser and plasma conditions.

Nonlinear saturation of these instabilities sets in when a surface ripple grows to $\sim 1/2$ laser wavelength. Figure 2 presents three snapshots of the interaction region near 2.4 ps in 150 fs intervals. Figures 2(a)–2(c) show the laser Poynting flux normal to the plasma surface, which, together with the corresponding electrostatic field E_z , drops over a skin depth. The force by the electromagnetic field tensor component in the lateral direction is much smaller than along the irradiation direction. When a surface modulation reaches the scale of a laser wavelength, as shown in Fig. 2(b), its side wall is not supported as much and plasma pressure wins. This leads to the emission of plasma in the lateral direction (y axis); see Fig. 2(b) at $y > 3 \mu\text{m}$. Emitted electrons and ions are weakly magnetized in the emission’s magnetic field ≥ 130 MG along the plasma surface, so that a layer of plasma at a density near n_c forms near the surface over a few microns. While plasma is advected away from the surface and density drops, the frozen-in magnetic field is losing strength. At the end of the plasma emission [see Fig. 2(c)] the ripple is “deflated,”

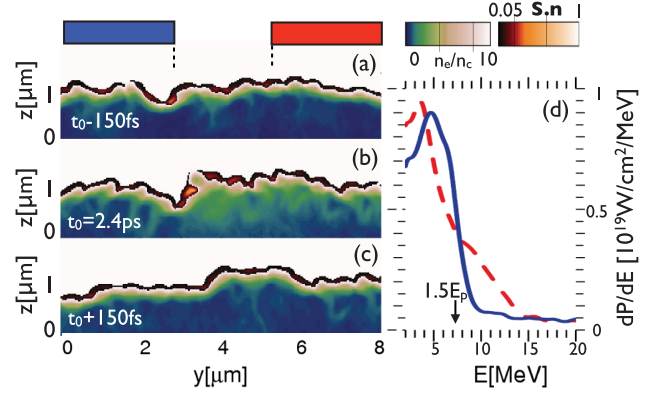


FIG. 2 (color). Nonlinear saturation stage of plasma surface rippling driven by the laser interaction; (a)–(c) snapshots of laser Poynting flux $|\mathbf{S}_\perp|$ normal to the $n_e = 10n_c$ surface in red and electron density in green, around the time 2.4 ps when plasma is emitted—quantities averaged over two laser cycles; (d) electron energy spectra at 2.4 ps determined in regions with and without prior emission of plasma, as indicated by the colored boxes in top of (a).

leading to an effective stabilization of the surface. As a consequence, the surface recedes without much pressure buildup in the dense plasma. Tracking the location where the laser is absorbed, we find that the surface moves at a near-constant velocity $v_s \simeq 5 \times 10^{-3}c$ along the laser direction; compare Fig. 1. This velocity can be derived from momentum conservation between the impinging laser, plasma electrons, and bulk ions [6]. In our case, a large fraction $f_a = 0.7$ – 0.8 of the incident laser momentum I_0/c is absorbed into relativistic electrons, different from Ref. [6] where $f_a \ll 1$. Including the reflected light, the total momentum on the laser side is $(2 - f_a)I_0/c$. To satisfy momentum balance between laser and plasma, the ions need to carry a small fraction $(2 - 2f_a)I_0/c$. Hence, the momentum balance between the laser pulse $I_0/c \equiv a_0^2 n_c m_e c^2 / 2$ and that absorbed in the plasma gives $2(1 - f_a)a_0^2 n_c m_e c^2 / 2 = 2M_i n_i v_s^2$, where n_i is the bulk ion density, in agreement with the velocity observed in our simulation.

The nonlinear saturation of the surface rippling leads to the generation of three groups of fast electrons via distinct absorption mechanisms.

(1) For a clean plasma-density step, absorption is dominated by particles that originate in the overdense plasma region. Electrons enter the vacuum region by means of their thermal velocity inside the bulk plasma and get accelerated in the standing-wave pattern of the laser electromagnetic fields in front of the surface. Their excursion length is a fraction of a laser wavelength before they are pushed back into the target, where they cease to interact with the laser; as a result, their energy is limited by the ponderomotive energy; the energy spectrum has a cutoff near $1.5E_p = 7$ MeV for $a_0 = 10$ [9,10]. The corresponding energy spectrum is shown by the blue curve in Fig. 2(d), which

represents a region where the density profile is very steep, i.e., not affected by emission of plasma from density ripples. Figure 3 describes the evolution of electron energy spectra over 5 ps, determined $3 \mu\text{m}$ behind the laser interaction region and corresponding transversely averaged density profiles in the laser spot region. By 2 ps the steep part of the density profile, where the first group of electrons is generated, assumes a scale length of $l_p = 0.15 \mu\text{m}$ between n_c and $10n_c$ where the laser is absorbed. This scale is given by the Debye length for density $n_e = a_0 n_c$ and temperature $kT = a_0 m_e c^2$ [17], so $l_p = \sqrt{a_0 m_e c^2 / (4\pi e^2 a_0 n_c)}$, which we have confirmed by separate 2D simulations at various intensities and initial plasma gradient lengths. The scale length l_p is independent of laser intensity and initial conditions of the plasma but depends on laser wavelength alone. Emission of plasma from the target surface modifies this idealized scenario in that of-order 100 MG magnetic fields are generated by surface currents and deflect electrons with subponderomotive energies, so that the net electron energy flux behind the plasma surface drops locally by up to 50%.

(2) Laser interaction with the plasma emitted by deflating surface ripples, which extends as a density plateau just below n_c over several microns from the surface, as shown in Fig. 3(b), can accelerate particles to energies beyond E_p . This produces a second group of electrons, shown in more

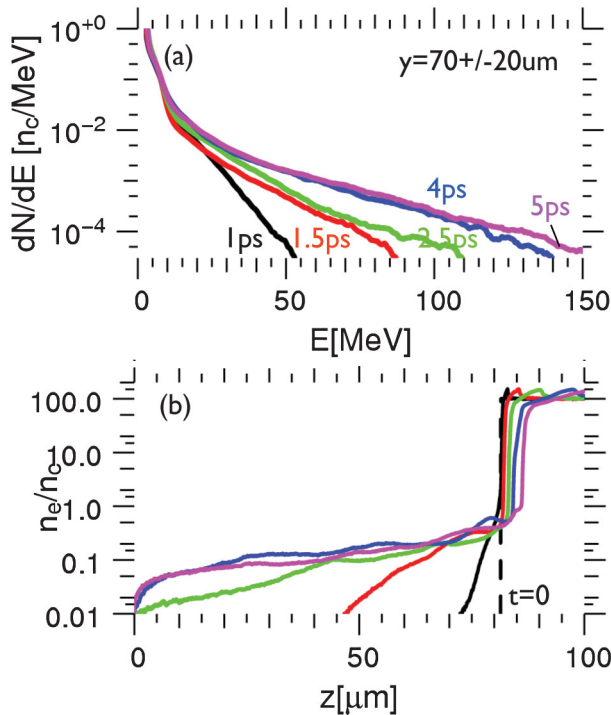


FIG. 3 (color). (a) Energy spectra of laser-generated electrons consist of three energy groups, with a high-energy tail that asymptotes at 4 ps; (b) similarly, electron density profiles, averaged across the laser spot, asymptote towards a near plateau at 4 ps; colors in (a) and (b) for the same time steps match.

detail in Fig. 2(d), where one can see a strong increase in the production of electrons with energies between 7 and 15 MeV when the electron spectrum is measured behind the plasma emission (dashed line), compared to one measured behind a location with no recent emission (solid line). On average, the plasma emission yields a hotter spectrum than expected from a density step, because the distance over which some electrons interact with the laser is extended compared to the clean interface.

(3) While the first two mechanisms occur over a sub-picosecond time scale, the emission of particles from the target surface leads to filling of the vacuum region in front of the target with underdense plasma over several picoseconds. Direct laser acceleration of electrons [8] in this region gives rise to a third group of electrons with energies up to 150 MeV after ≈ 4 ps in the case considered here. The plasma density profile flattens with time and reaches a scale length of $40 \mu\text{m}$ in which electrons are accelerated over tens of microns into a Boltzmann-like spectrum with a slope $T_{\text{eff}} = 1.5(I_{\text{laser}}/10^{18} \text{ W/cm}^2)^{1/2} \approx 17 \text{ MeV}$ [8], which is much greater than expected from ponderomotive scaling. The density profile resembles an isothermal rarefaction $n_e(z, t) = n_{e,0} \exp(-z/c_s t)$ with a sound velocity $c_s = \sqrt{(m_e c^2 / M_i) a_0} \approx 0.05c$ and an electron temperature $a_0 m_e c^2$ determined by the laser amplitude. Over a wide range of laser intensities, we observe $n_{e,0} \approx (0.15 \pm 0.03)n_c a_0^{1/2}$, with the prefactor determined by details of the surface emission. The power driving such an expansion $8m_p n_{e,0} c_s^3$ amounts to only 1% of the incident laser power [18]. Because of the finite laser spot size, the expansion remains one-dimensional until its scale length exceeds the size of the laser spot, i.e., at $r_0/c_s \approx 2$ ps, which explains the asymptotic scale length of underdense plasma being similar to the laser spot diameter observed in our simulation.

Figure 1(b) shows that the outer edge of the laser beam is evolving due to whole-beam self-focusing, so that the conditions at the edge over a length $\approx \lambda_L$ are different from the interior. As the relative volume of edge filaments in 2D (3D) is $(2\lambda_L/R)$, their role is small for a wide beam.

The distinction between these energy groups and the characterization of their histories has been verified by tracking test particles in our simulation. Numerical convergence has been verified with simulations at a spatial resolution of 150 cells per wavelength in a $24 \times 75 \mu\text{m}$ simulation box, giving quantitatively similar results. Plasma background heating was found to agree between the 50 and the 150 cells per wavelength cases. Note that a transverse simulation box width of less than ten wavelengths, in which the number of spatial surface modes is limited, will lead to an underestimation of the surface emission effect; the same holds for unrealistic ion mass. The robustness of the emission mechanism has been verified by similar simulations at $4\times$ higher and $4\times$ lower intensity, where we find consistent results for absorption fraction as well as energy partition in terms of the parameter E_p .

For applications of petawatt lasers like fast-ignition ICF, we discuss the energy distribution of the laser-generated electron beam as a function of time and its divergence more quantitatively. Figure 4 compares the net forward energy flux of laser light through the injection plane to the energy flux of the electron beam through a plane behind the absorption interface. The net laser energy flux peaks at 0.6 ps before it is reduced by reflected light; the time lag between the laser and electron flux is due to the finite distance between the injection plane and target surface. At 1 ps, the fraction of energy coupled into the first group of “ponderomotive” electrons is 25% of the laser power; this value drops with time due to pump depletion of the laser in expanding plasma. The fraction of energy that goes into superponderomotive electrons rises to nearly 45% as the vacuum region in front of the target fills with plasma. The scale length of underdense plasma grows until ~ 4 ps and saturates at around the laser spot size. Electrons in this long underdense plasma are accelerated up to 150 MeV [8]. From the net laser energy flux through the injection plane, we find that up to 80% of the injected light is absorbed into energetic electrons.

The difference between electron energy flux and net laser flux in Fig. 4 is due to the divergent nature of the electron beam, which is caused by geometrical effects as well as by magnetic fields near the target surface. Even in the case of an idealized plasma density step, laser-accelerated electrons have a finite angular distribution, because of the short distance over which they are accelerated and due to beam filamentation in overdense plasma [4,5]. On top of that, magnetic fields that originate in the

emission of plasma from the target surface deflect electrons, because the Larmor radius of a 7 MeV electron in a 100 MG field is less than $3 \mu\text{m}$, which is similar to its acceleration distance. When these fields advect away from the surface, they become less forceful; at the same time, the most energetic electrons are accelerated over tens of microns, so they are more forward-directed. In our 2D simulation the angular distribution of energy flux, determined from a sum over particles n in the plane $[z_0, z_0 + L_z]$ behind the laser spot whose velocity vectors are within the angular interval $[\theta, \theta + \Delta\theta]$ with respect to the laser direction

$$\frac{\Delta P_e(\theta)}{\Delta\theta} = \frac{m_e c^2}{L_z \Delta\theta} \sum_{n \in \mathbb{A}(z, \theta)} |v_{e,n}| (\gamma_n - 1) n_{e,n} \quad \text{with}$$

$$\mathbb{A}(z, \theta) \equiv \{n | z_0 \leq z_n \leq z_0 + L_z;$$

$$\theta \leq \tan^{-1}(p_{y,n}/p_{z,n}) \leq \theta + \Delta\theta\} \quad (1)$$

and $\gamma_n \equiv \sqrt{1 + |p_n|^2}$, where p_n is the momentum of particle n , has a Gaussian shape with a $1/e$ width of approximately 1 rad.

Comparing the reference case shown above to a three-dimensional (3D) simulation for a laser spot that is scaled by one-half with similar laser and target conditions, we find that 2D results for laser polarization in the simulation plane are essentially a central cut through an equivalent 3D run. However, an important feature observed only in three-dimensional simulations is the isotropization of the forward-moving electrons in the plane perpendicular to the laser propagation axis. In 2D cartesian simulations, particles cannot gain momentum perpendicular to the simulation plane for symmetry reasons.

In conclusion, we have studied the interaction of realistic petawatt laser pulses with overdense plasma for several picoseconds, using kinetic particle-in-cell simulations in two and three dimensions to extend by an order of magnitude beyond what is experimentally accessible today in terms of laser energy. We find that laser interaction causes perturbations of the plasma interface giving up to 80% absorption into energetic electrons. Nonlinear saturation of these perturbations leads to recurrent emissions of plasma from the target surface which stabilize the surface while keeping absorption continuously high. Laser power is converted into three distinct groups of energetic electrons with energies up to several times the ponderomotive potential. Steady absorption into electrons around the ponderomotive energy, i.e., < 7 MeV for $a_0 = 10$, at a 25% level has important implications for fast ignition, where 1–3 MeV electrons deposit their kinetic energy to the dense core of a compressed ICF pellet. In order to shift the electron energy spectrum towards lower energies at a given short-pulse laser power, one could either reduce laser intensity while increasing the spot size, as suggested by scaled simulations, or move to frequency-doubled light.

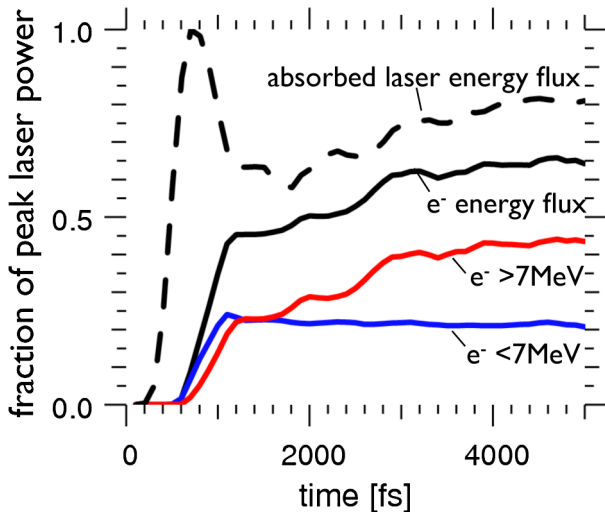


FIG. 4 (color online). Time history of energy partition in laser-generated electrons, showing sustained absorption of up to 80% (absorbed laser energy flux through $z = 0$ plane, dashed line) into relativistic electrons (total electron energy flux projected on z , solid black line); also shown are contributions from particles with energies $E_{\text{kin}} \leq 1.5E_p = 7$ MeV and > 7 MeV; all values are normalized to peak laser power $P_L \equiv 1.3$ PW.

We thank M. Tabak, B. Cohen, M. Key, Y. Sentoku, D. Strozzi, and P. Patel for discussions and encouragement. Computing support for this work came from the LLNL Institutional Computing Grand Challenge program. This work was performed under the auspices of the U.S. Department of Energy by the Lawrence Livermore National Laboratory under Contract No. DE-AC52-07NA27344.

-
- [1] C. P. J. Barty, *Nucl. Fusion* **44**, S266 (2004).
[2] W. Theobald *et al.*, *Phys. Plasmas* **18**, 056305 (2011).
[3] J. Kawanaka *et al.*, *J. Phys. Conf. Ser.* **112**, 032006 (2008).
[4] J. C. Adam, A. Héron, and G. Laval, *Phys. Rev. Lett.* **97**, 205006 (2006); B. Chrisman, Y. Sentoku, and A. J. Kemp, *Phys. Plasmas* **15**, 056309 (2008); J. Tonge, J. May, W. B. Mori, F. Fiuza, S. F. Martins, R. A. Fonseca, L. O. Silva, and C. Ren, *Phys. Plasmas* **16**, 056311 (2009); B. F. Lasinski, A. B. Langdon, C. H. Still, M. Tabak, and R. P. J. Town, *Phys. Plasmas* **16**, 012705 (2009); C. Ren *et al.*, *Phys. Rev. Lett.* **93**, 185004 (2004).
[5] Y. Sentoku, K. Mima, S. Kojima, and H. Ruhl, *Phys. Plasmas* **7**, 689 (2000).
[6] S. C. Wilks, W. L. Kruer, M. Tabak, and A. B. Langdon, *Phys. Rev. Lett.* **69**, 1383 (1992).
[7] F. Brunel, *Phys. Fluids* **31**, 2714 (1988); P. Gibbon and E. Förster, *Plasma Phys. Controlled Fusion* **38**, 769 (1996).
[8] A. Pukhov and J. Meyer-ter-Vehn, *Phys. Rev. Lett.* **76**, 3975 (1996).
[9] A. J. Kemp, Y. Sentoku, and M. Tabak, *Phys. Rev. E* **79**, 66406 (2009).
[10] J. May, J. Tonge, F. Fiuza, R. Fonseca, L. Silva, C. Ren, and W. Mori, *Phys. Rev. E* **84**, 025401 (2011).
[11] S. Atzeni and M. Tabak, *Plasma Phys. Controlled Fusion* **47**, B769 (2005).
[12] H. Ruhl, in *Introduction to Computational Methods in Many Body Physics* (Rinton, Paramus, NJ, 2006).
[13] A. G. MacPhee *et al.*, *Phys. Rev. Lett.* **104**, 055002 (2010).
[14] C. Birdsall and B. Langdon, *Plasma Physics via Computer Simulations* (Institute of Physics, Bristol, 1991).
[15] Y. Sentoku, K. Mima, P. Kaw, and K. Nishikawa, *Phys. Rev. Lett.* **90**, 155001 (2003).
[16] D. an der Bruegge, N. Kumar, A. Pukhov, and C. Rödel, *Phys. Rev. Lett.* **108**, 125002 (2012); A. Macchi, F. Cornolti, and F. Pegoraro, *Phys. Plasmas* **9**, 1704 (2002); E. G. Gamaly, *Phys. Rev. E* **48**, 2924 (1993); E. J. Valeo and K. G. Estabrook, *Phys. Rev. Lett.* **34**, 1008 (1975); H. Nishimura, K. Mima, Y. Yanase, N. Banjaya, H. Fujita, K. Iba, M. Matoba, S. Nakai, and C. Yamanaka, *Plasma Phys.* **22**, 69 (1980); R. Z. Sagdeev, in *Plasma Physics and the Problem of Controlled Thermonuclear Reactions*, edited by M. A. Leontovich and J. Turkevich (Pergamon, London, 1959).
[17] The relativistic Debye length is, to within a factor of the order of unity, identical to the classical expression; see G. Manzke and D. Kremp, *Physica (Amsterdam)* **97A**, 153 (1979).
[18] S. Atzeni and J. Meyer-ter-Vehn, *The Physics of Inertial Fusion* (Oxford University, New York, 2004).